Acta Materialia 255 (2023) 119092

Contents lists available at ScienceDirect

Acta Materialia

journal homepage: www.elsevier.com/locate/actamat

Full length article

Long-distance interface diffusion induced non-volume-conserved deformation in self-supported submicron-sized aluminum pillars

Degang Xie [a,*], Rongrong Zhang [a], Xiaohan Dai [a], Zhiyu Nie [a], Xinyao Wang [a], En Ma [a,c], Ju Li [b], Zhiwei Shan [a,*]

[a] Center for Advancing Materials Performance from the Nanoscale (CAMP-Nano), State Key Laboratory for Mechanical Behavior of Materials, Xi'an Jiaotong University, Xi'an 710049, China
[b] Department of Nuclear Science and Engineering and Department of Materials Science and Engineering, Massachusetts Institute of Technology, Cambridge, Massachusetts 02139, USA
[c] Center for Alloy Innovation and Design (CAID), State Key Laboratory for Mechanical Behavior of Materials, Xi'an Jiaotong University, Xi'an 710049, China

ARTICLE INFO

Keywords:
Plasticity
High temperature deformation
Coble creep
Whisker growth
Oxide layer
Aluminum

ABSTRACT

The plastic deformation of a solid generally conserves the local mass/volume of the sample. Here, we show that under elevated temperature and low strain rate, this may not hold for the widely used compression test geometry with self-supported aluminum pillars in the submicron range. Plastic flow can instead proceed with continuous shortening, while the overall diameter and shape remain constant. This apparent non-conservation results from a rarely-reported interface-diffusion-mediated deformation, when interface diffusion between the metal and the native oxide layer is rejuvenated to mediate mass relocation spreading over an interfacial area far exceeding the dimensions of the self-supported pillar, thus providing large continuous plastic strain.

1. Introduction

In recent decades, the increasingly widespread applications of micro-/nano- electromechanical systems and miniaturized devices have spurred the investigation of plastic deformation behavior in small-volume materials. For materials with dimensions in the micron- and sub-micron regimes, the specimen size can strongly alter the mechanical property, as best exemplified by the famous tenet of “smaller is stronger” [1,2]. Smaller can also be much weaker at even smaller sample sizes [3,4]. Fundamentally, such a strong size dependence originates from the interplay between two basic plasticity mechanisms, i.e., the displacive plasticity and the diffusional plasticity [4]. The displacive plasticity, also known as low-temperature plasticity, is mediated by dislocation glide and deformation twinning, where the atomic registries change in a collective and semi-deterministic manner, whereas in diffusional plasticity, such as Coble creep or Nabarro-Herring creep [5], atoms change their registries individually in a randomized manner to form a diffusional flow. In experimental studies of small-scale deformation mechanisms, self-supported pillars [6] have been widely employed, where both types of plasticity come into play, as exemplified either by the slip step on the sample surface caused by dislocation slip [1,7,8] or by mushrooming of a compressed pillar due to stress-gradient-driven diffusion near the loading site [9–11]. In other words, during mechanical deformation of these self-supported samples, atoms exchange positions within the pillar-shaped sample, while the total sample volume/mass is conserved. In what follows, we show that atoms can travel a long distance, at least tens of times farther than sample dimensions, via diffusion along an interface, in contrast to more commonly seen diffusional deformation where atoms only travel a distance limited by the external dimensions of the sample [12]. Actually, similar long-distance diffusional deformation has been hinted in previous observations of tin or cadmium whisker formation [13], with frequent observations that after days of natural aging, the internal stress in deposited films can drive massive diffusion of atoms, possibly along the dislocations/grain boundaries/interfaces, to energetically favorable surface sites that are tens or hundreds of micrometers away, leading to the growth of whiskers [14–16]. Compared with bulk materials, small volume materials have much higher surface/interface area to volume ratio, thereby making such defect-mediated long-distance diffusion easier to happen, and such diffusion can readily exceed the small external geometrical sizes. When a self-supported sample is deformed via this long-distance diffusional plasticity, conservation of local sample

---

* Corresponding authors.
E-mail addresses: dg_xie@xjtu.edu.cn (D. Xie), zwshan@xjtu.edu.cn (Z. Shan).

https://doi.org/10.1016/j.actamat.2023.119092
Received 10 October 2022; Received in revised form 11 April 2023; Accepted 11 June 2023

volume would seem to break down, rendering the deformation mode abnormal in contrast to the well-known small-scale plastic deformations with conserved local volume.

In this work, we examine interface-diffusion-mediated liquid-like plasticity by mimicking the condition of Sn whisker growth [13,14,16], which requires a high homologous temperature (>0.5TM, TM is the bulk melting temperature) and slow deformation rate. Therefore, we choose compression tests of sub-micron sized single-crystalline aluminum pillars under increasing homologous temperatures (up to 0.72TM) and decreasing strain rates (down to 10^{-3} s^{-1}). We select aluminum as the experimental material for several reasons: Firstly, aluminum naturally possesses a compact native oxide layer that is strongly adhered to the metal matrix and remains chemically stable even under high vacuum, high temperature and mechanical deformation [17,18]. Therefore, this oxide layer provides a unchanged pathway for interface diffusion along the metal/oxide interface. Additionally, the thin oxide layer is also known to be ductile and able to follow the deformation of the metal substrate to a high strain without breakup [18–20].

2. Experimental methods

Sample preparation. Single crystal aluminum (99.9995%) disks were cut into 1.5 mm × 2 mm rectangular plates, which were mechanically polished to 100 μm in thickness and electrochemically thinned to a few microns at one edge. Submicron-sized cylindrical pillars and rectangular pillars were prepared by milling with a focus ion beam (FIB, FEI Helios NanoLab 600, operating at 30keV) on the thinned edge. The milling current used in the final step was as low as ~20 pA to minimize geometrical tapering and irradiation damage caused by the ion beam. The thickness of the surface-affected layer was about 5 nm, according to the TEM observation. All pillars had an aspect ratio (top diameter/length) of 1/2~1/3.5. The cylindrical pillars had a taper angle of 2°~4°, while the rectangular pillars had a taper angle of less than 1°.

***In situ* annealing and thermomechanical tests.** The in situ TEM heating and compression tests were performed using a heater device mounted onto a Bruker Hysitron PI95 PicoIndenter holder in an environmental TEM (Hitachi H9500, operating at 300kV and 0.5~4 μA emission current). The crystal orientation of the pillar axis is <110> and the electron-beam direction is <001> for all the tested pillars. The heating and compression tests were carried out subsequently in vacuum $<10^{-4}$ Pa. To minimize the influence of different configurations of preexisting dislocations induced by FIB processing, all samples were pre-annealed at 400 ℃ to a pristine state before the tests at various temperatures and strain rates. The Hysitron PI95 holder comes with a diamond punch connected to a MEMS transducer, which has a force resolution of ~ 300 nN and displacement resolution of ~2 nm. We use displacement control to apply a constant loading rate. The drift of the tip and substrate were measured from the video using Matlab code and used to rectify the original displacement data. The effect of the electron beam on the specimen temperature is less than one degree Celsius [21–23], and the engineering stress-strain curve without electron illumination nearly overlaps with that under normal tests, indicating that the effect is negligible [9].

3. Results and discussion

3.1. Compression of cylindrical pillars

Fig. 1 displays the deformation behavior of a set of aluminum pillars with similar diameters of 168 to 220 nm, which were compressed at similar strain rates of ~10^{-3} s^{-1} but at different temperatures. The engineering stress-strain curves shown in Fig. 1a indicate that as the testing temperature rises, the plastic deformation becomes more and more smooth and continuous, accompanied by the decrease of yield or flow-stress. At 100 ℃, the deformation assumes a distinctive displacive character, starting with a stiff linear segment of elasticity until reaching a high strength of ~2.3 GPa, immediately followed by a huge strain burst. When the testing temperature increases to 200 ℃, we still observe the elasticity and the strain burst, but with an extra continuous segment in between. This continuous segment has been proven to be due to diffusional plasticity in our previous work [9]. As the temperature further increases to 275 ℃, the strain burst disappears from the stress-strain curve and is replaced by a few small serrations, indicating a relatively mild displacive plasticity, possibly due to its much lower flow stress insufficient to trigger the large-scale correlated dislocation emission. However, at 400 ℃, even those small serrations vanish from the engineering stress-strain curve throughout the whole strain range up to 50%. Unlike the three other curves with clear yield points, the engineering stress-strain curve at 400 ℃ is quite smooth and continuous without an obvious yield point, implying a rather blurred transition from elasticity to plasticity at a low stress level. After ~10% strain, the plastic flow proceeds almost steadily along a stress plateau at ~600 MPa, despite a weak "strain hardening" originating from the tapered sample geometry, which dictates an increasingly larger diameter of oxide shell at the ripple-forming site and also a bigger deformation volumn of the internal metal crystal as the compression proceeds.

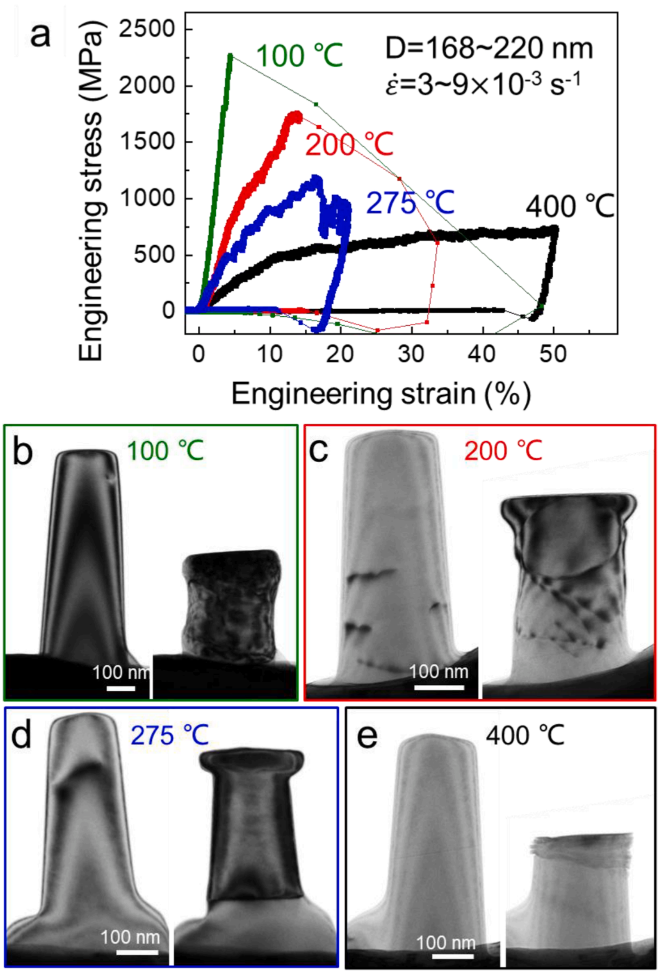

Fig. 1. The effect of temperature on the compressive deformation of a group of pillars with similar diameters≈200 nm tested under a strain rate≈3~9×10^{-3} s^{-1}. (**a**) Engineering stress-strain curves for four pillars tested at different temperatures between 100 ℃ and 400 ℃. (**b-e**) Comparison of pillar morphology before and after compression test. The test temperatures are marked with the same color as the corresponding engineering stress-strain curve in (a).

The changes of sample morphology before and after the compression, as shown in Fig. 1b-e, also demonstrate a similar transition of deformation mechanism with temperature. In these post-compression images, dislocation-dominated displacive plasticity signified by slip steps on the surface (Fig. 1b and 1c) occurs at relatively low temperature, while at relatively high temperature, diffusional plasticity [9] becomes increasingly obvious, as evidenced by the formation of a mushroom-shaped top (Fig. 1c and 1d). At the intermediate temperatures of 200 ℃ and 275 ℃, the plasticity is of a mixed displacive/diffusional type, displaying both the mushroomed top and slip step. However, at 400 ℃, the 50% compression strain did not result in shear-off, mushrooming, or a uniform increase of the pillar diameter, implying an abnormal plasticity mechanism. However, there were a few wrinkles of the oxide shell at the top of the pillar (Fig. 1e), indicating that some metal originally encased by this oxide shell had been emptied, such that the volume may not have been conserved during deformation. According to volume conservation, the pillar diameter should have increased by 41% at a height reduction of 51%, but we did not observe a significant increase in diameter, suggesting a dramatic reduction in volume during compression. In conventional mushrooming process, deformation mainly occurs in the upper segment of the pillar near the loading site, described as short-distance diffusional plasticity. However, in the 400 ℃ case, we will demonstrate that the abnormal plastic deformation is mediated by long-distance diffusion over a much larger area; it will thus be referred to as long-distance diffusional plasticity in the later discussion.

This type of non-volume-conserved deformation can also be seen in another sample observed with a higher TEM magnification (see Fig. 2 and Supplementary Movie 1). Aside from the similar engineering stress-strain curve (Fig. 2a) and deformed morphology (Fig. 2b and 2c), we also found no appreciable deformation-induced increase in the pillar diameter, as evidenced by perfect overlay of the deformed pillar profile with the white dashed line representing the original pillar profile. Our further characterization shown in Fig. 2d-e indicates that after compression, the pillar remains cylindrical with a clean and intact surface oxide layer, thus precluding the possibility of compression-induced extrusion or change of cross-section shape. We note here that the pillar is connected to the substrate, and is in contact with the loading punch in the experimental setup. Therefore, to ensure scientific rigor, we checked whether Al could have been leaked to these connected objects. For this purpose, these connected objects have been inspected and compared before and after the compression test in a larger viewing field under SEM (see Fig. 3). The comparison results show that both the loading punch and the vicinity of the pillar exhibit nearly identical surface morphology before and after the test, so that the possibility of mass leakage can be excluded. Another evidence to preclude the occurrence of mass leakage is shown in Fig. 4, where metal extrusion is observed during compression. In the engineering stress-strain curve in Fig. 4a, a sudden load drop at about strain≈17% can be observed, which can be correlated with the unexpected rupture of the oxide shell. In the subsequent compression test, the compression stress remained at a low level (<300 MPa at $\dot{\varepsilon}$=~0.01 s^{-1}), which can be attributed to the existence of this broken hole in the oxide shell. However, in most compression tests, we didn't find such a load drop and subsequent plasticity at decreased stress level, indicating that the oxide shell should have remained intact throughout the compression test and thus no mass leakage though the oxide shell occured.

In addition, we also performed experiments to check whether the continous shortening of the pillar is due to the sink-in effect of the metal core during compression. We compressed an aluminum pillar with dispersed Al_3Sc particles, which can be used as reference markers to characterize the movement of the pillar interior. As can be seen in Fig. 5, the position of these precipitate particles remains unchanged during compression, so that sinking of the pillar into the matrix can be excluded. Uniform shortening of the pillar can also be ruled out by this experimental result.

One obvious change observed during this apparent non-volume-conserved deformation is the wrinkling of the oxide shell near the pillar top. As shown in Fig. 1e and Fig. 2c, e and f, the oxide shell near the pillar top appears to be corrugated and form multiple wrinkles stacked on top of each other during compression, similar to the

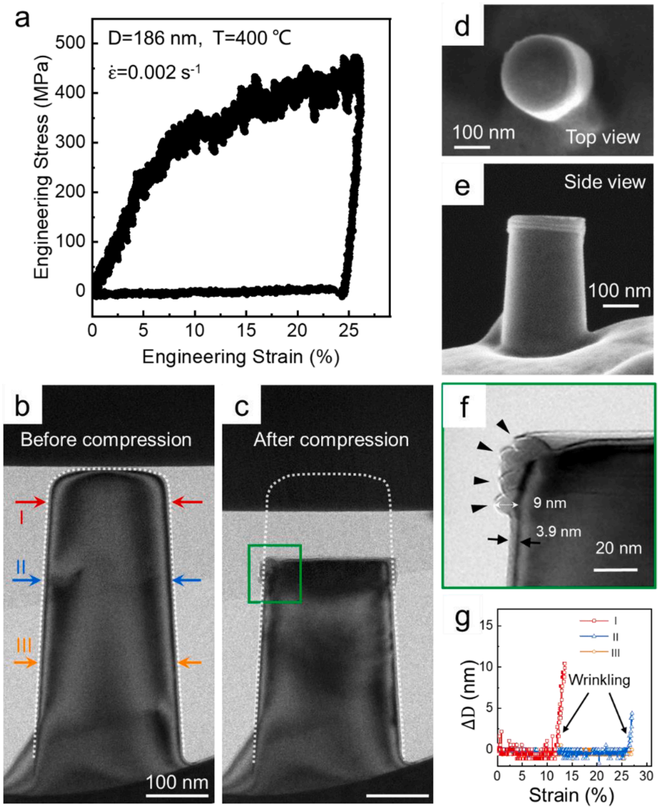

Fig. 2. Typical compressive deformation of a cylindrical pillar with diameter D=186 nm at a high temperature of 400 ℃ and a low strain rate $\dot{\varepsilon}$=0.002 s^{-1}. See also Supplementary Movie 3. (**a**) The engineering stress-strain curve. (**b**) and (**c**) are images of the pillar before and after the compression, respectively. The profile of the pillar in (b) is indicated by a white dash line, which is superimposed in (c). (**d**) and (**e**) are SEM images of the deformed pillar, viewed from the top and from the side, respectively. (**f**) Magnified view of the area indicated by the green box in (c) to show the wrinkling of the native oxide layer, as indicated with black triangle markers. (**g**) the change in projected width of the pillar with compression strain, extracted with Matlab from the recorded video (Supplementary Movie 3) at 3 positions indicated in (b).

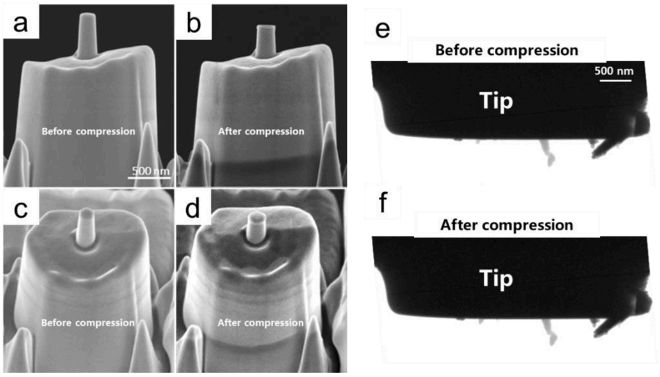

Fig. 3. Comparison of the surface morphology near the pillar and the profile of the loading tip before and after the compression test. (**a-d**) are SEM images of the pillar and the base viewed from the side direction (a-b) and from ~45°off the top direction. (**e-f**) are TEM images of the tip viewed from the side.

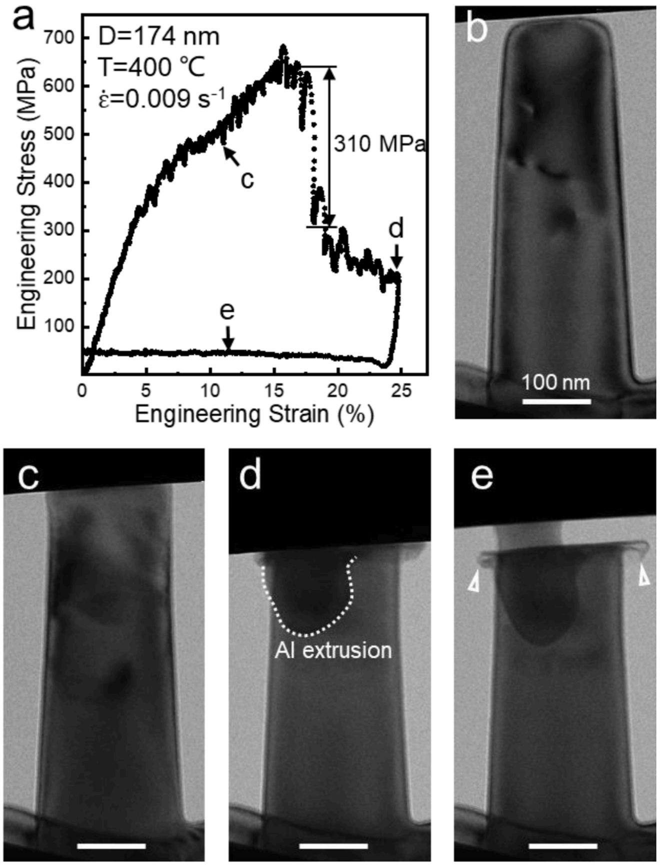

Fig. 4. Extrusion of aluminum metal from the oxide shell observed during a compression test. (**a**) the engineering stress-strain curve. (**b-e**) serial images show the deformation at different moments as indicated in (a). Extrusion of aluminum is shown in (d). White triangles in (e) indicate the oxide wrinkles at the top of the pillar.

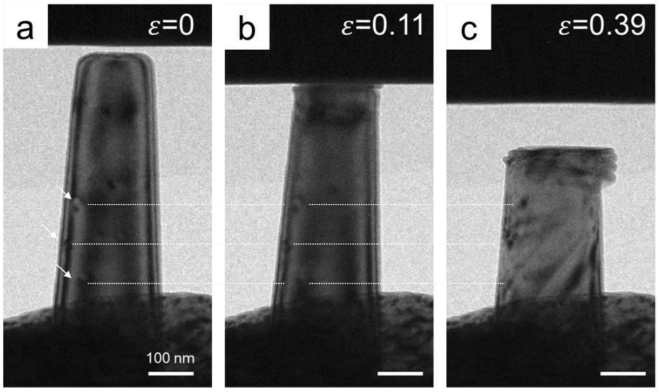

Fig. 5. Compression of an aluminum alloy pillar with embedded $AlSc_3$ particles. (**a-c**) are the evolution of pillar profile with the compression strain, which is indicated in the upper-right corner. Three white dashed lines are drawn horizontally to indicate the initial position of three particles in (a), which are marked with white arrows to verify whether these particles move with the compressive deformation. All scale bars represent 100nm.

compression of a bellows. The type of wrinkle formation in a core/shell cylinder can be attributed to surface instability, which occurs when the a critical axial strain is exceeded [24]. During compression, as shown in Supplementary Movie 1, wrinkles are generated one by one as the compression proceeds. The generation of each oxide wrinkle requires an increase in compression displacement of approximately 18 nm, which is roughly equal to the increase in oxide layer thickness at the wrinkled part. This indicates that the original metal atoms inside the wrinkle-forming oxide shell have been continuously removed, and the resulting excess area of oxide shell is folding up to form the wrinkles. In our experiments, the departing atoms have two choices in diffusion path, either through the bulk or the metal/oxide interface. In general, the diffusivity of aluminum at the surface/interface/grain boundary diffusivity is at least 4 orders of magnitude higher than the diffusivity of the bulk at a given temperature [25,26], and is therefore the preferred choice. The wrinkling mechanism of the oxide shell observed in our study differs from that observed in Yang's work [20]. In their experiments, surface wrinkles were also formed during pillar compression at room temperature. However, unlike our study where wrinkles were generated one by one as the compression proceeded, multiple wrinkles appeared nearly at the same pace in Yang's work. The formation mechanism was attributed to mismatched deformation across the metal/oxide interface and did not involve significant diffusional plasticity.

In the textbook, deformation mediated by interface diffusion is explained by Coble creep theory. When a cylindrical pillar is compressed, a stress gradient $\Delta\sigma_{nn}$ can build up along the interface from the compressive region at the contact point to the adjacent stress-free region. This stress gradient can naturally induce interface diffusion, driving diffusional plasticity. As the diffusing atoms leave the compression site and squezz into interfaces to make their way forward, a pressure/stress can be generated along the diffusion path that may cause morphological changes, such as an increase in the diameter of the cylindrical pillar. To determine if this is the case, we analyzed the recorded deformation video to track the possible deviation of the measured diameter from the initial value at three fixed positions, as labeled in Fig. 2b. This digital measurement provides a high spatial resolution of ~0.5 nm, which corresponds to the thickness of two {111} surface layers. It is therefore precise enough to detect the growth of one atomic layer on either side or a tiny elastic deformation of the oxide shell (1% stretch of oxide shell can cause ~1.4 nm increase of the overall diameter). As can be seen from Fig. 2g, the overall diameters at all three positions exhibit no increase within the measurement resolution, indicating that the deformation of the oxide layer is far below its elastic strain limit and that the oxide layer inflates outward by at most one atomic layer. Such a small increase in the pillar diameter has important implications. First, it suggests that the interfacial atomic flux responsible for the observed plasticity exerts only a weak stress or pressure in most interface regions. The deformation strain of the oxide shell along the circumferential direction ($\varepsilon <$ 0.5nm/186nm= 0.26%) resulting from such a weak internal stress is within the elastic regime. The elastic deformation of the oxide shell can exert a pressure acting on the metal core, the value of which can be derived from the classical hoop stress for a core/shell cylinder equation in classical mechanics [27]:

$$\Delta \mathrm{P} = \sigma_h \cdot 2t/D \tag{1}$$

where σ_h is the hoop stress ($=E_{oxide}\bullet\varepsilon$=350GPa×0.5nm/186nm=0.9 GPa), t and D are the thickness of the oxide shell and the diameter of the tube/pillar (for the pillar in Fig. 2, t=5nm, D=186nm). Then, we can estimate the maximum pressure difference ΔP across the oxide shell generated by the interfacial atomic flux to be ~48 MPa. Given that the pillar was tested under high vacuum, ΔP represents the maximum stress/pressure carried by the atomic flux. Second, it means that the inflowing aluminum atoms have not even formed a complete atomic layer under the oxide shell of the pillar. However, for the neighboring flat region where there is no hoop constraint as in the cylindrical pillar, we can not rule out the possibility that the incoming atoms may form new atomic layers that can lift up the entire oxide layer. However, if we assume that the atoms from the original compression volume have spread out as a monolayer disk in the flat region, we can have an opportunity to roughly estimate the diffusion range of interfacial atoms. By simple geometric equivalence, the diameter of the resulting "monolayer disk" (D_{ML}) can then be estimated using the following equation:

$$D_{\mathrm{ML}} = \sqrt{\frac{H \cdot \varepsilon}{d_0}} \cdot D \tag{2}$$

where D and H are the diameter and height of the pillar, ε is the compression strain and d_0 is the thickness of the monolayer (d_0=0.234 nm for a (111) monolayer of Al). Inserting the parameters for the three pillars, the diameters of the corresponding monolayer disks are calculated to be 4~12 μm, which is tens of times of the pillar size. Given the atoms spread along the interface sparsely, forming a "layer" with thickness far less than a monolayer, the atoms leaving the deformation volumn have traveled a diffusion range that is much larger than the calculated diameters. Such a long diffusion range is in contrast to the diffusion range within the pillar volumn in the well-known mushrooming-type diffusional plasticity. For this reason, the diffusion responsible for the observed plasticity in our experiments can be reasonably named as long-distance interface diffusion.

3.3. *Compression-induced metal extrusion*

The next step is to verify the existence of atomic flux at the interface triggered by the pillar compression. Direct visualization of the atomic flow along the interface and the subsequent redeposition at a weak site is challenging using the current *in situ* TEM technique. As an alternative, we performed another compression experiment using a cylindrical pillar with a preset hole in the oxide shell, which could serve as a redeposition site. The hole is created by scratching the loading tip at a location on the cylindrical surface about 150 nm from the top surface, immediately prior to the compressive loading to minimize oxidation of the newly exposed metal. The compression results are shown in Fig. 6 and Supplementary Movie 2. We observed that during the loading stage, Al atoms leak out from the hole and redeposit to form a small hillock, which changes its shape with increasing size, possibly due to surface reconstruction (Fig. 6d). In the subsequent unloading stage, the extruded metal is immediately sucked back into the pillar. However, by carefully correlating the stress-strain curve and the movie clip of the "suck-back" process, we found that in the initial unloading stage with a stress drop from the peak stress to zero, the metal hillock almost remains unchanged, but in the subsequent tip-pillar separation stage, where a "negative pressure" is generated by the adhesive pulling on the top of the pillar, the hillock is quickly sucked into the pillar. Apparently, the "negative pressure" enabled an backward flow of atoms along the interface from the hillock to the metal/oxide interface at the top of the pillar. Consequently, both the formation and the "suck-back" process of the hillock observed in this experiment demonstrate that the stress gradient can drive an atomic flux along the interface, where atoms seek weak sites along the diffusion path to relocate themselves.

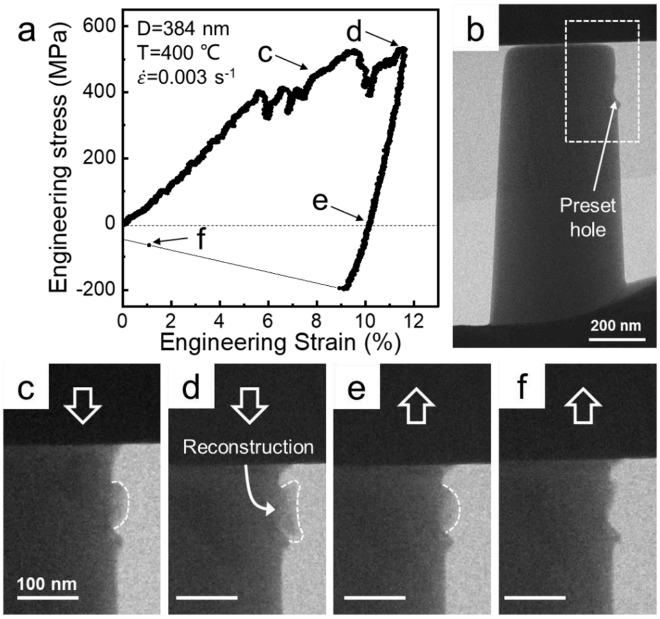

Fig. 6. The compression test of an aluminum cylindrical pillar with a preset hole at the side surface. See also Supplementary Movie 4. (**a**) The engineering stress-strain curve of the pillar with a diameter D=384 nm at 400 ℃ and strain rate $\dot{\varepsilon}$=3.0×10^{-3} s^{-1}. (**b**) is the bright-field TEM image of the pillar before compression test. (**c-f**) are the serial images of the area bounded by the white-dashed box in (b), which are extracted from the video at moments indicated in (a), to show the extrusion of metal from the preset hole during compression test. The profile of the extruded metal is indicated by a white dotted line, and the white arrows at the top of the images represent the moving direction of the loading punch.

The cylindrical pillar used in the above experiment has a circular cross-section, and thus exhibits strong hoop confinement. However, because our estimated range of interface diffusion during compression tests far exceeds the dimensions of the pillar sample, most of the atoms must have diffused into the adjacent interface area, which is generally flat and loosely confined. For this reason, we performed *in situ* nanoindentation into the flat aluminum surface with a similar preset hole about 300 nm away from the engagement site. As shown in Fig. 7 and Supplementary Movie 3, metal extrusion and the suck-back action are also observed during indentation and retraction, respectively.

Both the pillar compression result and the nanoindentation result indicate that the metal atoms diffuse along the interface and seek weak spots to re-deposit. In our previous experiments, we observed occasional removal of aluminum atoms from the interior of the pillar and the formation of cavities primarily at the corner site when we kept the pillar at a high temperature for a long time (like 1 hour), and much more frequently (nearly 100%) when the interface was weakened by hydrogen [28]. The formation of cavities at high temperature indicates that there are many empty sites at the interface for the incoming atoms to deposit due to defects, internal stress, or local deformation near the interface. However, in our experiments, the loading only takes a few tens of seconds, which is much faster than the tens of minutes required for the heating-induced cavitation process. Therefore, compressive loading still played a major role in driving the diffusional deformation observed in our experiments. Intrinsically, such interfacial atomic flow and redeposition are driven by the difference in chemical potential associated with the stress state. The potential difference can transmit a long distance with little attenuation, resulting in a slow yet steady atomic flux.

Based on the above experimental results, we suggest that non-volume-conserved deformation is mediated by a mild interfacial atomic flow tending to leave the area of compressive stress, not only along strongly-confined interface such as cylindrical wall, but also along loosely-confined interface such as the flat surface. The exiting atoms travel along the metal/oxide interface until finding a redeposition site. Potential redeposition sites are areas where extra space is available, such as defects, voids or surface indents. Due to the strong elastic confinement from the oxide shell, each redeposition site can only accommodate a limited number of metal atoms, thus necessitating a large area to provide an adequate number of redeposition sites to accommodate all the atoms exiting from the compressed part. As a result, the oxide shell only feels a small stress and deforms in the elastic regime, resulting in a seemingly abnormal deformation without conserving the volume of the local pillar. Since the deformation happens in a uniformly distributed manner in an area much larger than the pillar itself, no appreciable changes in size and shape of cross-section areas of the cylindrical pillar are expected. The total mass/volume is actually conserved if one counts all the Al spreading over the supporting substrate.

3.4. *Effects of electron beam irradiation, pillar diameters and strain rates*

Since the observed continuous shortening deformtion of the pillars is

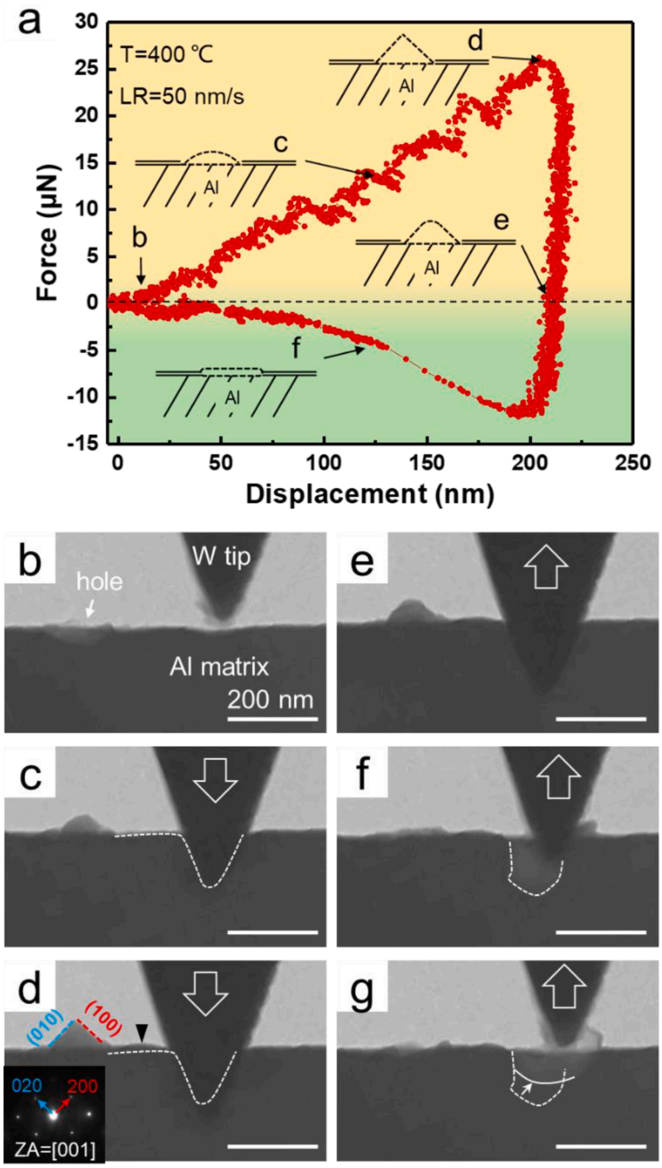

Fig. 7. Nanoindentation test at 400 ℃ into the surface of Al, which has a preset hole about 300 nm away from the loading site. See also Supplementary Movie s5. (**a**) the force-displacement curve of the indentation test. (**b-g**) is a series of snapshots extracted from the movie at the moments as indicated with arrows in (a). (b) is the profile of the sample before engaging the tungsten indenter tip, with a preset hole indicated with an arrow. The white arrows in (c-g) indicates the directions of the indenter motion. (b-d) is a loading session showing the extrusion of metal from the hole, followed by the formation of a hillock. The hillock underwent the Wulff reconstruction assuming two low-index facets, as indicated with blue and red dashed lines in (d). The insert in (d) is a diffraction pattern of the aluminum substrate indicating the zone axis is [001] and loading direction [110]. The surface contour of the aluminum in (c) is marked with the white dashed line and is superimposed in (d) as a reference. (e-g) As the indenter retracted, the hillock sank into the metal and the surface of the indent partly recovered, as indicated by the change from the white dashed line to the white solid line in (f) and (g). All scale bars represent 200nm.

mediated by long-distance interface diffusion, the irradiation effect from high voltage electron beam also need to be excluded [29,30]. Fig. 8 shows the results of the beam-on/off experiments. These results indicate that under our experimental conditions, the beam effect was not obvious. After turning off the electron beam, the aluminum pillar still exhibits a long-distance diffusional plasticity, resulting in a similar wrinkled shell at the pillar top.

The effect of pillar size on the deformation mechanism is shown in Fig. 9. The deformation of pillars with diameter less than 260 nm and strain rates 0.002~0.02 s^{-1} shows oxide wrinkles at the top of the pillar, indicating the domination of long-distance diffusional plasticity. However, for the pillar with diameter=312 nm and strain rate=0.006 s^{-1} shown in Fig. 9e, we observed slight mushrooming rather than wrinkling at the top of the pillar. This means that for tests at 400 ℃ and strain rate≈0.005 s^{-1}, the threshold diameter to activate the long-distance diffusional plasticity is 257-312 nm.

The effect of strain rate on the deformation mechanism is shown in Fig. 10, which is plotted with results of compression tests for pillars with simillar diameter D~180 nm at the same temperature=400 ℃, but under different strain rates from 0.002 to 0.5 s^{-1}. In Fig. 10, we can find a threshold strain rate ≈0.01 s^{-1}, across which the engineering stress-strain curves change from smooth to serrated, and the deformed morphology of these pillars from continuous shortening to shear-off. These changes across the threshold strain rate clearly indicate the transition in plastic defromation from the mechanism of displacive plasticity to long-distance diffusional plasticity.

We present here only an example group of experiments to show the effects of strain rates and pillar sizes. In real situations, the specific plasticity mechanism of pillar deformation depends on three experimental parameters, namely pillar size, temperature and strain rate. If we set any two of the three experimental parameters to fixed values, we can always find a threshold value for the third parameter at which the plasticity mechanism transition occurs. With a sufficient number of testing results, a deformation mechanism map (DMM) can be constructed showing the regimes of different deformation mechanisms and the transition boundaries in between. An example of such a DMM is shown in Fig. 11. In the diffusional plasticity region of this DMM, a boundary between conventional diffusional plasticity and long-distance diffusional plasticity can also be roughly visualized.

3.5. *Compression of rectangular pillars*

In cylindrical pillars, the interfacial atomic flux experiences not only local confinement from the strong bonding to the compact oxide layer, but also overall confinement from the circular cross-section of the pillar, arising from the hoop stress against enlarging the enclosed area. Therefore, if we change to a pillar with non-circular cross-section, the overall confinement is expected to be much weaker, because the cross-section shape can evolve towards a circle to help relieve the internal pressure. To verify this prediction, two pillars with rectangular cross-section and nearly the same equivalent diameter were compressed at 400 ℃. Two different strain rates were applied to generate different levels of internal pressure/stress. From the results shown in Fig. 12, similar wrinkling phenomenon was observed at a slower strain rate (~0.008 s^{-1}), while at a relatively high strain rate (~0.03 s^{-1}), mushrooming of the pillar top happened. However, there are several key differences: first, both engineering stress-strain curves (Fig. 12a) contain obvious serrations, which were not observed in those curves of cylindrical pillars shown in Fig. 1 and Fig. 2. Second, the wrinkles are larger than those in deformed cylindrical pillars, leading to an increase of the pillar width by over 50 nm, compared to ~18 nm in the cylindrical pillar. As demonstrated in Fig. 12b-d and Supplementary Movie 4, the 70% compressive strain has generated about 10 wrinkles on the surface (nearly ~40 nm displacement per wrinkle), which roughly matches the number of serrations in the stress-strain curves, indicating an intermittent nature in the yielding of the oxide shell. Obviously, it is the generation of larger wrinkles that has led to the serrations in the stress-strain curve in rectangular pillars. Also, as more wrinkles stack together, a larger extra stress is required to create a new wrinkle at a location further away from the contact interface, thus resulting in the strain hardening observed in the stress-strain curve. Third, in the high-strain rate compression, as demonstrated in Fig. 12e-h and Supplementary Movie 5, the deformation forefront of the shell, as marked with

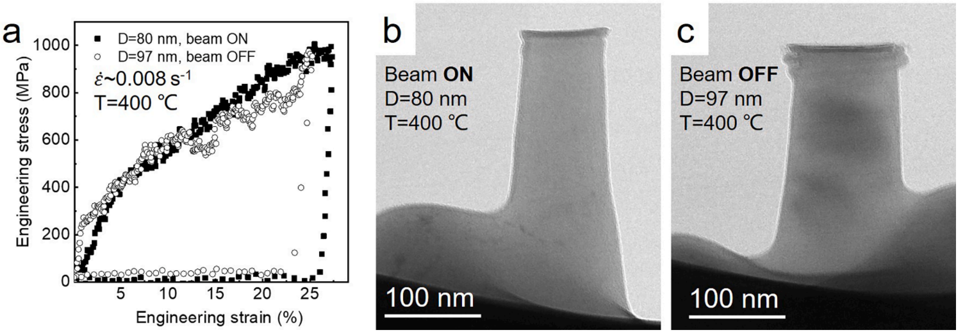

Fig. 8. Effect of the electron beam irradiation on the long-distance diffusional plasticity. (a) the engineering stress-strain curves for two aluminum pillars tested under beam-on and beam-off conditions, respectively. (b) and (c)show the shapes of the two deformed pillars.

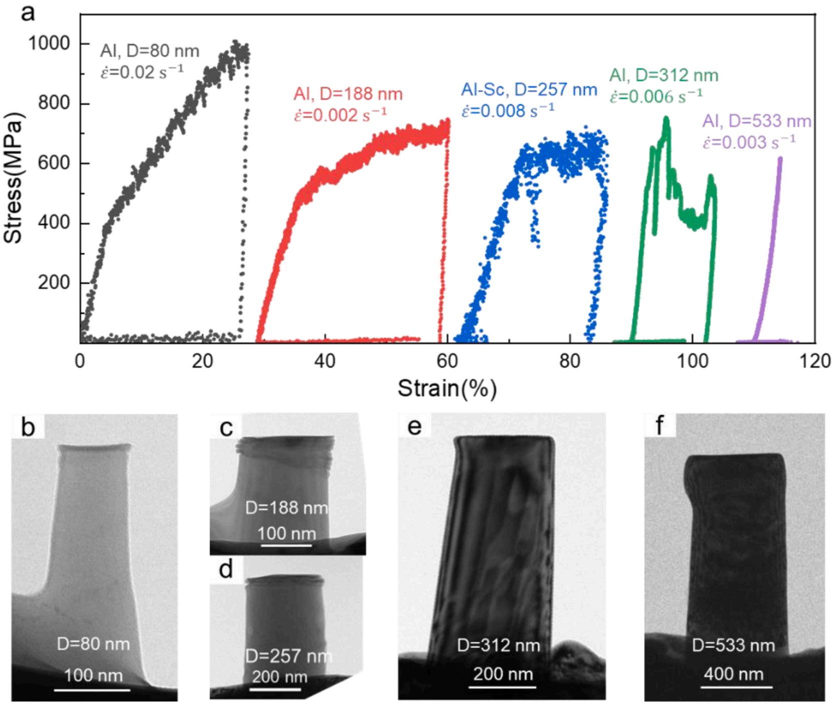

Fig. 9. The influence of pillar diameter on the deformation mechanism at 400 ℃. (a) The engineering stress-strain curves for compression of pillars with different diameters. (b-f) Morphology of the deformed pillars with different diameters.

black triangles in Fig. 12f-g, can extend much farther than in the compression of cylindrical pillars (see Fig. 1). This location of the deformation front actually reflects the difference in overall confinement between circular and rectangular cross-section. The cross-sectional area of the rectangular pillar can be easily increased by transforming towards a circular shape while maintaining a constant perimeter through local yield at the four corners under stress/pressure. Fig. 12i and 12j provide an example comparing cross-section shape before and after compression of a rectangular pillar. In contrast, the cylindrical pillar requires global yielding of the circular cross-section to increase the enclosed area, requiring higher stress such that the deformation forefront locates closer to the loading site.

4. Summary

Based on the above findings, the deformation behavior of submicron-sized aluminum with native oxide shell can be summarized as follows. With increasing test temperature or decreasing strain rate, the sample deformation can be successively dominated by four types of plasticity mechanisms, i.e., the stochastic displacive plasticity, the diffusional-displacive plasticity, the short-distance diffusional plasticity, and the long-distance diffusional plasticity, as illustrated in Fig. 13. Displacive plasticity mediated by dislocation slip or twinning usually generates slip steps or deformation bands, resulting in poor deformation controllability for samples on micrometer scale. For the coupled diffusional-displacive plasticity (Fig. 13b), the diffusional deformation happens at relatively low stress level, followed by the activation of displacive plasticity at stress concentration sites. Further increase in deformation temperature or decreasing strain rates can lead to full diffusional plastic deformation (Fig. 13c and 13d), which have two forms that differ by the diffusion distance. At relatively lower testing temperatures or higher strain rates, atoms flowing in the interface become jammed within a small volumn near the contact zone, generating an internal pressure that causes the oxide layer to bulge to form a mushroom-shaped pillar (Fig. 13c). However, under relatively high testing temperature or low strain rate, atoms can slowly diffuse to a much longer distance due to exponentially higher diffusivity with *T*↑, seeking easy sites to relocate themselves with minimal energy expense. Potential relocation sites for deposition of incoming atoms may include a surface hole, a preexisting cavity in the interface, or other types of imperfections along the

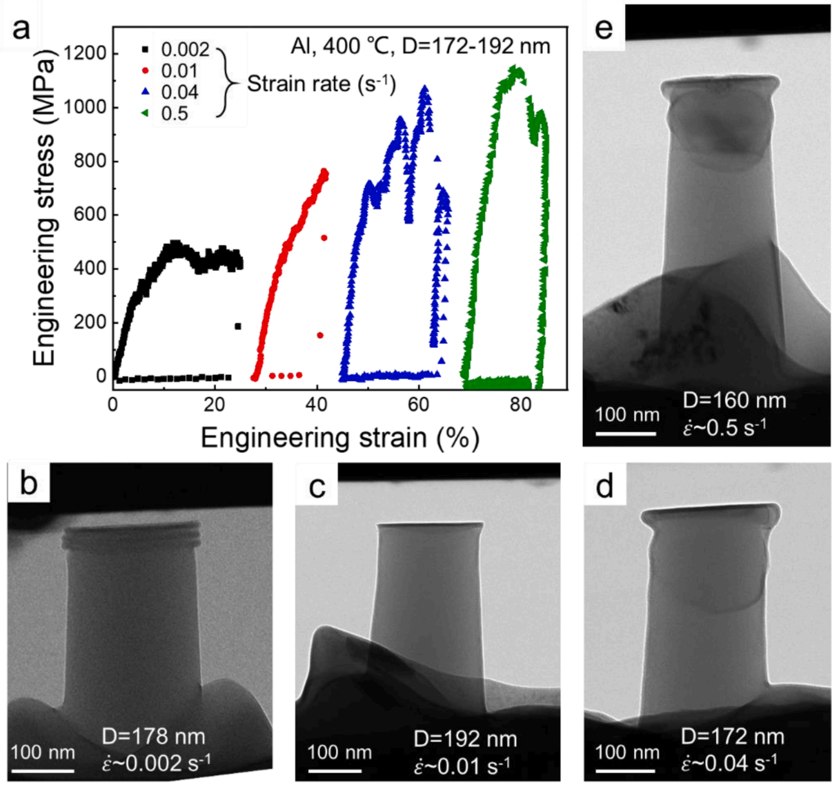

Fig. 10. The dependence of plasticity mechanisms on strain rate during compression of aluminum pillars with diameters of 172-192 nm at 400 ℃. (a) The engineering stress-strain curves for compression of pillars at different strain rates. (b-e) Morphology of the deformed pillars compressed at different strain rates.

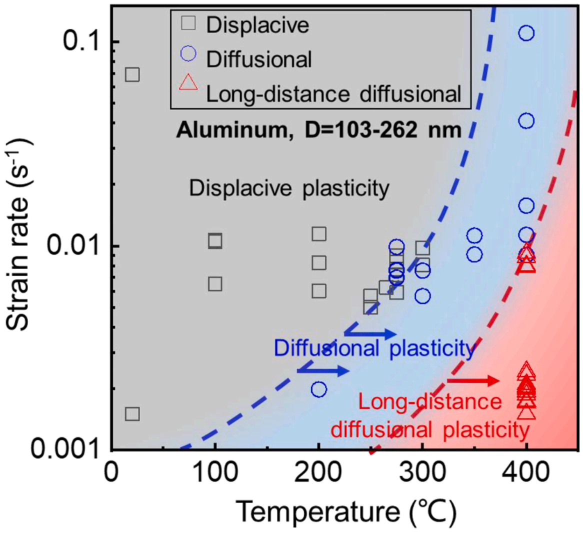

Fig. 11. The deformation mechanism map for aluminum pillars with diameter=103-262 nm.

interface. With this type of long-distance diffusional plasticity, there is no appreciable change in shape even near the loading site, and the volume is not conserved within the pillar sample itself during the deformation (Fig. 13d). Nevertheless, when taking a much larger area into consideration, the volume and mass of the sample (including substrate) are actually conserved; it is just that they are redistributed over a distance far beyond the dimensional scales of the pillar. Similar behavior of long-range transport and deposition of metal was seen in solid-state lithium metal battery [31] where the local volume was not conserved.

In conclusion, we have systematically studied the deformation of sub-micron sized aluminum pippars with a native oxide layer. The results demonstrate that by decreasing strain rate or increasing temperature, the deformation behavior of the pillar can change from a stochastic type (displacive type), to a continuously mushrooming type (short-distance diffusional type), and ultimately, to a continuously-distributed type (long-distance diffusional type). The latter two types of diffusional plasticity can impart impressive reshaping capability of small-volume materials due to the synergistic contribution from the high surface/interface diffusivity and the small length scale of diffusion. Upon choosing an appropriate deformation rate and temperature, the small-volume metals may deform through a coupled plasticity mechanism, providing superb deformability comparable to semi-solid metal forming. Moreover, it is worth noting that the long-distance diffusional deformation does not instigate obvious shape change near the loading site, but instead relocates the exiting atoms across a much larger area by filling up interfacial "holes". These characteristics of the long-distance diffusional deformation can be potentially exploited for strengthening the metal/oxide interface near the loading site (within microns at least), or for tuning the pillar length without obviously changing the surface morphology or apparent size, which may be useful, for example, in pillar-array-based optical applications [32–34].

CRediT authorship contribution statement

Z.S. and D.X. designed the project. **R.Z., X.W., X.D. and Z.N.** conducted the experimental work. **X.W., X.D. and D.X.** analyzed the data. **D.X.** wrote the paper with the input from **Z.S., J.L., and E.M.**. All authors contributed to discussions of the results.

Additional Information

Correspondence and requests for materials should be addressed to D. X..

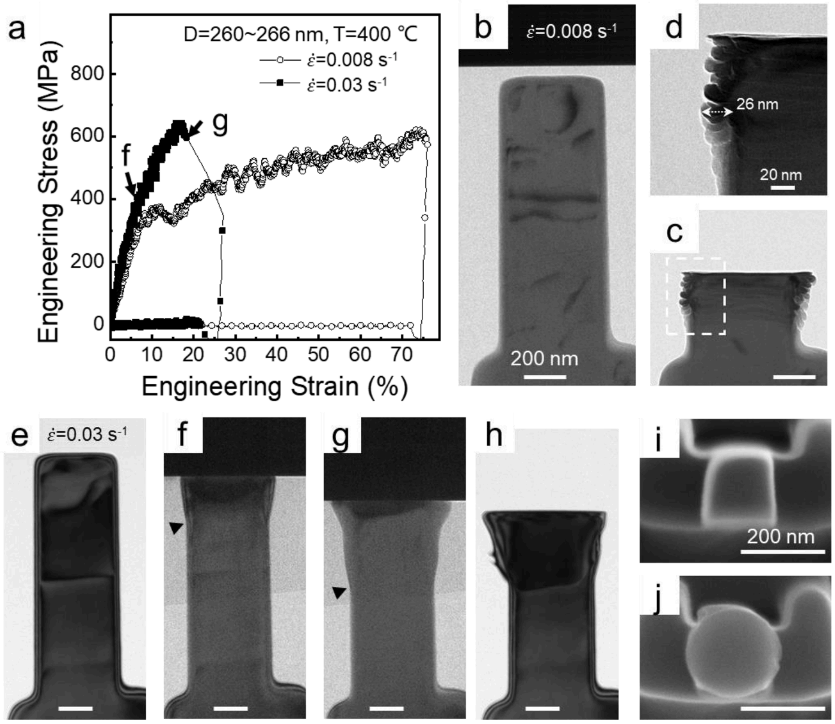

Fig. 12. Compression tests of aluminum pillars of similar equivalent diameter of ~260 nm with rectangular cross-section at 400 ℃ and different strain rates. (**a**) Engineering stress-strain curves of two pillars tested at a low strain rate of 0.008 s^{-1} and a high strain rate of 0.03 s^{-1}, respectively. (**b**) and (**c**) are bright-field TEM images before and after low-strain-rate compression. The area marked with a white dashed box in (d) is enlarged and shown in (**d**). (**e**-**h**) are video snapshots of sample deformation during high strain rate compression. (e) and (h) were taken before and after the compression, while (f) and (g) at moments labeled in (a). The black triangle indicates the front line of the deformation. (**i**) and (**j**) are SEM images taken from the top of a pillar (D≈192 nm) before and after compression at 275 ℃ and strain rate of 0.008 s^{-1}, to show the shape change of cross-section in the deformed part.

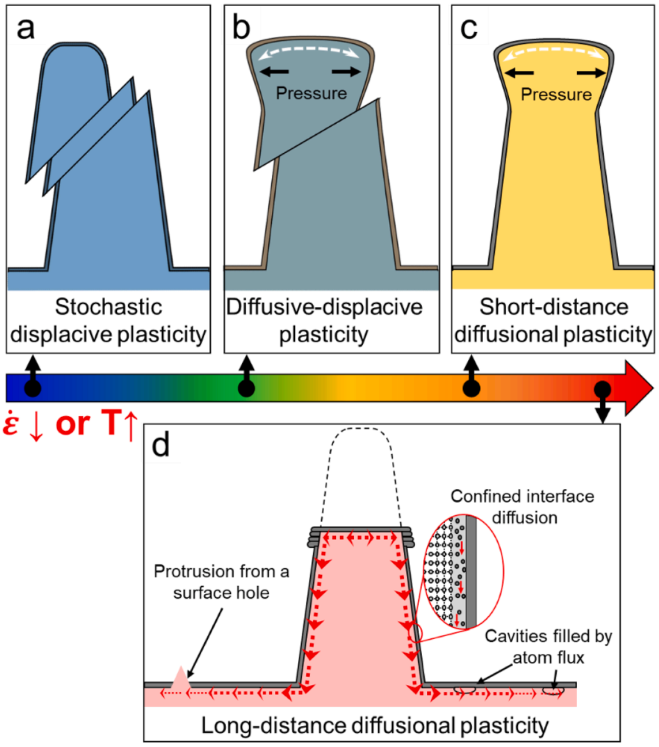

Fig. 13. Schematic illustration of the evolution of deformed shape from displacive plasticity to long-distance diffusional plasticity, as the temperature and strain rate change. (**a**) At high strain rate and low temperature, displacive plasticity dominates, resulting in slip bands or slip steps in the pillar. (**b**) shows the deformation governed by diffusional-displacive plasticity. (**c**) shows the deformation resulted from short-distance diffusional plasticity, which inflated up the pillar locally at the top. (**d**) At relatively high temperature and slow strain rate, long-distance diffusional plasticity occurs, producing a corrugated pillar profile.

Declaration of Competing Interest

The authors declare no competing financial interests.

Acknowledgements

We acknowledge Q. Q. Fu and D. L. Zhang for assistance in focused ion beam and TEM experiments. D. Xie and Z. Shan acknowledge supports from Natural Science Foundation of China (52031011 and 51971169), Shaanxi Postdoctoral Science Foundation (2017JQ5110). J. Li acknowledges support by NSF CBET-2034902.

Supplementary materials

Supplementary material associated with this article can be found, in the online version, at doi:10.1016/j.actamat.2023.119092.

References

[1] M.D. Uchic, D.M. Dimiduk, J.N. Florando, W.D. Nix, Sample dimensions influence strength and crystal plasticity, Science 305 (2004) 986–989.
[2] Q. Yu, Z.-W. Shan, J. Li, X. Huang, L. Xiao, J. Sun, E. Ma, Strong crystal size effect on deformation twinning, Nature 463 (2010) 335–338.
[3] L. Tian, Z.-W. Shan, E. Ma, Ductile necking behavior of nanoscale metallic glasses under uniaxial tension at room temperature, Acta Mater 61 (2013) 4823–4830.
[4] L. Tian, J. Li, J. Sun, E. Ma, Z.W. Shan, Visualizing size-dependent deformation mechanism transition in Sn, Scientific Reports 3 (2013) 2113.
[5] R.L. Coble, A model for boundary diffusion controlled creep in polycrystalline materials, J. Appl. Phys. 34 (1963), 1679-&.
[6] A.M. Minor, G. Dehm, Advances in in situ nanomechanical testing, MRS Bull. 44 (2019) 438–442.
[7] Q. Yu, L. Qi, T. Tsuru, R. Traylor, D. Rugg, J.W. Morris, M. Asta, D.C. Chrzan, A. M. Minor, Origin of dramatic oxygen solute strengthening effect in titanium, Science 347 (2015) 635–639.
[8] G. Dehm, B.N. Jaya, R. Raghavan, C. Kirchlechner, Overview on micro- and nanomechanical testing: New insights in interface plasticity and fracture at small length scales, Acta Mater 142 (2018) 248–282.
[9] D.-G. Xie, R.-R. Zhang, Z.-Y. Nie, J. Li, E. Ma, J. Li, Z.-W. Shan, Deformation mechanism maps for sub-micron sized aluminum, Acta Mater 188 (2020) 570–578.
[10] J.M. Wheeler, C. Kirchlechner, J.-S. Micha, J. Michler, D. Kiener, The effect of size on the strength of FCC metals at elevated temperatures: annealed copper, Philos. Mag. 96 (2016) 3379–3395.

[11] C.Q. Chen, Y.T. Pei, J.T.M. De Hosson, Effects of size on the mechanical response of metallic glasses investigated through in situ TEM bending and compression experiments, Acta Mater 58 (2010) 189–200.

[12] J. Sun, L.B. He, Y.C. Lo, T. Xu, H.C. Bi, L.T. Sun, Z. Zhang, S.X. Mao, J. Li, Liquid-like pseudoelasticity of sub-10-nm crystalline silver particles, Nat. Mater. 13 (2014) 1007–1012.

[13] G.T. Galyon, Annotated tin whisker bibliography and anthology, IEEE Transactions on Electronics Packaging Manufacturing 28 (2005) 94–122.

[14] W.J. Choi, T.Y. Lee, K.N. Tu, N. Tamura, G.T.T. Sheng. Structure and kinetics of Sn whisker growth on Pb-free solder finish. Electronic Components & Technology Conference, 2002.

[15] W.J. Boettinger, C.E. Johnson, L.A. Bendersky, K.W. Moon, M.E. Williams, G. R. Stafford, Whisker and hillock formation on Sn, Sn–Cu and Sn–Pb electrodeposits, Acta Mater 53 (2005) 5033–5050.

[16] B.Z. Lee, D.N. Lee, Spontaneous growth mechanism of tin whiskers, Acta Mater 46 (1998) 3701–3714.

[17] J.M. Schneider, A. Anders, B. Hjörvarsson, I. Petrov, K. Macák, U. Helmersson, J.-E. Sundgren, Hydrogen uptake in alumina thin films synthesized from an aluminum plasma stream in an oxygen ambient, Appl. Phys. Lett. 74 (1999) 200–202.

[18] Y. Yang, A. Kushima, W. Han, H. Xin, J. Li, Liquid-like, self-healing aluminum oxide during deformation at room temperature, Nano Lett 18 (2018) 2492–2497.

[19] F.G. Sen, A.T. Alpas, A.C.T. van Duin, Y. Qi, Oxidation-assisted ductility of aluminium nanowires, Nature communications 5 (2014).

[20] Y. Yang, S.Y. Wang, B. Xiang, S. Yin, T.C. Pekin, X. Li, R. Zhang, K. Yano, D. Hwang, M. Asta, C. Grigoropoulos, F.I. Allen, A.M. Minor, Evaluating the effects of pillar shape and gallium ion beam damage on the mechanical properties of single crystal aluminum nanopillars, J. Mater. Res. 36 (2021) 2515–2528.

[21] J. Silcox, M. Whelan, Direct observations of the annealing of prismatic dislocation loops and of climb of dislocations in quenched aluminium, Philos. Mag. 5 (1960) 1–23.

[22] S. Kritzinger, E. Ronander, Local beam heating in metallic electron-microscope specimens, Journal of Microscopy-Oxford 102 (1974) 117–124.

[23] S.B. Fisher, On the temperature rise in electron irradiated foils, Radiat. EIT. 5 (1970) 239–243.

[24] Y. Tan, B. Hu, J. Song, Z. Chu, W. Wu, Bioinspired Multiscale Wrinkling Patterns on Curved Substrates: An Overview, Nanomicro Lett 12 (2020) 101.

[25] P. Shewmon, Diffusion in solids. Minerals, Metals & Materials Society, Warrendale, Pennsylvania, US (1989) 189–222.

[26] K.N. Tu, Fundamentals of Electromigration, Springer Ser Mater S, vol. 117 (2007) 211–243. Springer New York.

[27] G. Sinclair, J. Helms, A review of simple formulae for elastic hoop stresses in cylindrical and spherical pressure vessels: What can be used when, Int. J. Pres. Ves. Pip. 128 (2015) 1–7.

[28] M. Li, D.-G. Xie, E. Ma, J. Li, X.-X. Zhang, Z.-W. Shan, Effect of hydrogen on the integrity of aluminium–oxide interface at elevated temperatures, Nature Communications 8 (2017) 14564.

[29] S. Stangebye, Y. Zhang, S. Gupta, T. Zhu, O. Pierron, J. Kacher, Understanding and quantifying electron beam effects during in situ TEM nanomechanical tensile testing on metal thin films, Acta Mater 222 (2022).

[30] S.-H. Li, W.-Z. Han, Z.-W. Shan, Deformation of small-volume Al-4Cu alloy under electron beam irradiation, Acta Mater 141 (2017) 183–192.

[31] Y. Chen, Z. Wang, X. Li, X. Yao, C. Wang, Y. Li, W. Xue, D. Yu, S.Y. Kim, F. Yang, A. Kushima, G. Zhang, H. Huang, N. Wu, Y.-W. Mai, J.B. Goodenough, J. Li, Li metal deposition and stripping in a solid-state battery via Coble creep, Nature 578 (2020) 251–255.

[32] J. Zhu, Z. Yu, G.F. Burkhard, C.-M. Hsu, S.T. Connor, Y. Xu, Q. Wang, M. McGehee, S. Fan, Y. Cui, Optical absorption enhancement in amorphous silicon nanowire and nanocone arrays, Nano Lett 9 (2009) 279–282.

[33] L.P. Lee, Inspirations from biological optics for advanced photonic systems, Science 310 (2005) 1148–1150.

[34] M.L. Brongersma, Y. Cui, S. Fan, Light management for photovoltaics using high-index nanostructures, Nat. Mater. 13 (2014) 451–460.